# Towards a reliable assessment of charging effects during surface analysis: Accurate spectral shapes of ZrO2 and Pd/ZrO2 via X-ray Photoelectron Spectroscopy

Pascal Bargiela, Vincent Fernandez, Christophe Cardinaud, John Walton, Mark Greiner, David Morgan, Neal Fairley, Jonas Baltrusaitis

# Towards a reliable assessment of charging effects during surface analysis: accurate spectral shapes of $ZrO_2$ and $Pd/ZrO_2$ via X-ray Photoelectron Spectroscopy

**Pascal Philippe Bargiela,[1] Vincent Fernandez,[2] John Walton,[3] Mark Greiner,[4] David Morgan,[5] Neal Fairley,[6] and Jonas Baltrusaitis[7,*]**

[1]The Institute for Research on Catalysis and the Environment of Lyon (IRCELYON), 2 Avenue Albert Einstein, 69626 Villeurbanne, France
[2]Institut des Matériaux Jean Rouxel (IMN), Université de Nantes, CNRS, 2 rue de la Houssinière, BP 32229, 44322 Nantes cedex 3, France
[3]TSTC CIO, 5 Grosvenor Terrace, Teignmouth, TQ14 8NE UK
[4]Max-Planck Institute for Chemical Energy Conversion, Department of Heterogeneous Reactions / Surface Analysis Group, Mülheim an der Ruhr, Germany
[5]School of Chemistry, Cardiff University, Main Building, Park Place, Cardiff CF10 3AT, United Kingdom
and
HarwellXPS – EPSRC National Facility for Photoelectron Spectroscopy, Research Complex at Harwell (RCaH), Didcot, Oxon, OX11 0FA
[6]Casa Software Ltd, Bay House, 5 Grosvenor Terrace, Teignmouth, Devon TQ14 8NE, UK
[7]Department of Chemical and Biomolecular Engineering, Lehigh University, 111 Research Drive, Bethlehem, PA 18015, USA

## Abstract

X-ray Photoelectron Spectroscopy of large bandgap or insulating material surfaces relies on an effective mechanism that compensates for the emission (loss) of electrons by maintaining the material surface at a steady-state uniform potential. While a steady-state may be attained by utilizing an active compensation, such as low power electron emitting filament, there is the possibility that the surface potential is not uniform over the area analysed, leading to peak shifts and incorrect spectral interpretation. In this work, a spectral data processing method based on mapping the $ZrO_2$ and $Pd/ZrO_2$ surfaces utilizing photoemission peak binding energy is proposed, which provides information about the response of specific material surfaces to charge compensation. Spectromicroscopy of $ZrO_2$ and $Pd/ZrO_2$ surfaces without spatial information is used to monitor the efficacy of charge compensation. Exploiting counts distributed over many bins require the use of procedures and algorithms essential to practical mapping peak positions. Iterative singular value decomposition is therefore introduced and utilized as a means of efficiently delivering spatially resolved spectra from which binding energy for peaks is computed. The concepts developed in this work result in robust and accurate peak models of $ZrO_2$ and $Pd/ZrO_2$ that can be applied in XPS analysis of not only $ZrO_2$ but other large bandgap or insulating material surfaces. Supporting arguments for a peak model representing signal from Zr 3p and Pd 3d are developed within this work are presented.

*Corresponding author: job314@lehigh.edu; +1-610-758 6836

Keywords: XPS; $ZrO_2$; Pd/$ZrO_2$; charging; data processing; spectromicroscopy; peak model

## Introduction

Charge compensation is an essential part of any analytical technique that involves the emission of charged particles [1–3]. X-ray photoelectron spectroscopy (XPS) emits electrons and therefore must have a means of returning electrons to the material surface to prevent a constant build-up of positive potential [1]. For conducting material surfaces an effective connection to the ground is sufficient to maintain the material surface at a constant potential. However, for semiconducting or insulating material surfaces, a more involved charge replenishment mechanism must be deployed to prevent uncertainty in peak shapes that can potentially invalidate the chemical state determination for these material surfaces. The topic addressed here is the validation of charge compensation based on the use of imaging XPS via spectromicroscopy to yield accurate spectral lineshapes. The method described relies on mapping a surface in terms of photoemission peak position and in doing so identify related charging problems or confirms spectroscopic data contain valid chemical state information rather than artifacts of the measurement process. Mapping a surface via spectromicroscopy involves data treatment that permits measurement times acceptable to users and speed of analysis that encourages the use of these techniques. The method, therefore, describes in detail the algorithms used to facilitate the approach proposed using $ZrO_2$ and $Pd/ZrO_2$ as case studies.

In particular, $ZrO_2$ possesses a large bandgap ranging from 5.0 to 5.8 eV depending on the measurement technique [4]. It has been extensively utilized in surface catalyzed reactions alone [5] or as a support for various transition (noble) metals, such as Pd [6–10]. XPS analysis of materials with large band gaps, such as $ZrO_2$, requires charge compensation and therefore the problem of validating the quality of XPS data measured from material surfaces predominantly $ZrO_2$ is used as a case study with a positive outcome for the proposed methods. A powder form for material surfaces is used to illustrate how spectromicroscopy is applied to enhance confidence in spectroscopic data. These powderous material surfaces are routinely assumed to be uniform in composition over the analysis area therefore the expectation for imaging of these material surfaces is a set of images without any spatial information due to material surface composition. $ZrO_2$ also is an example of material where fitting of curves to data is essential. In particular, $ZrO_2$ presents an interesting case study because Zr 3p is an example of a doublet peak for which a simple approach to measuring photoemission signal above inelastically scattered background fails to yield the correct ratio for Zr $3p_{1/2}$ and Zr $3p_{3/2}$ intensities. Based on counting states allocated to quantum numbers j=1/2 and j=3/2, the ratio of these doublet peaks is expected to be 1:2. However calculating a background directly from data using the widely utilized Shirley algorithm [11] the ratio for the Zr 3p doublet peaks is approximately 2:3, therefore Zr $3p_{1/2}$ appears to be too intense relative to Zr $3p_{3/2}$. The complexity further increases when other peaks that overlap with Zr 3p, such as Pd 3d, are present in the measured XPS spectra [6–8].

Accurate interpretation of the Zr 3p envelope requires confidence in charge compensation coupled with an understanding of the shapes that must be modelled within the spectra.

This is explored using a successive spectromicroscopy experiments of $ZrO_2$ surface. The objective of this work is, thus, two-fold. First, the work focuses on deriving a spectromicroscopy approach for $ZrO_2$ surface charging monitoring while further developing a peak model accurately describing Zr 3p envelope in $ZrO_2$ with and without overlapping Pd 3d present is described.

## Materials and methods

### $ZrO_2$ and Pd/$ZrO_2$ synthesis

The 10% wt Pd supported on ZrO2 (MEL Chemicals, XZO 632/18, 90% Monoclinic-10% Tetragonal) was prepared by a deposition method, using a metal precursor solution of $Pd(OAc)_2$ in toluene. After heat treatment, the obtained solid was analysed by XPS.

### X-ray Photoelectron Spectroscopy (XPS)

XPS was performed on a Kratos Axis Ultra-DLD photoelectron spectrometer, using a monochromatic Al Kα radiation source operating at 144 W (12 mA × 12 kV) power. The Kratos Axis Ultra is equipped with a dual hemispherical analyser (HSA) arranged so that data can be collected either in energy dispersive mode (lower HSA) making use of the DLD as multiple detectors recording energy separated signal in parallel or operating as a spherical mirror (upper HSA) with the DLD operating as a 2D spatially resolved image detector acting as a single energy channel. Hybrid lens mode using a slot selected area aperture was used to acquire spectra via the lower HSA of the dual analyser Kratos Axis Ultra. High resolution and survey scans were performed at pass energies of 40 and 160 eV, with step sizes of 0.1 and 1 eV respectively. A magnetically confined charge compensation system was used to minimize material surface charging. Images were acquired making use of the upper HSA operating in lens mode FoV1 pass energy 40 eV.

Powder samples were mounted using carbon tape. Survey spectra show minimal C1s intensity suggesting the powder covered the tape sufficiently not to expose it.

Energy for electrons as recorded is dependent on the settings used for the charge compensation on Kratos Axis Ultra instruments. All spectra are displayed using the apparent binding energy for the given charge compensation settings. The exception occurs for data which are overlaid using a common binding energy scale. These overlaid data are systematically offset in energy to align the peak maximum for Zr $3d_{5/2}$ or Zr $3p_{3/2}$ as appropriate. Charge correction based on C 1s was not deemed appropriate as there was no evidence to support a ubiquitous uniform layer of adventitious carbon was present to provide a meaningful reference energy for calibrating the energy scale. Offsets in energy, when necessary, are consistently achieved through the use of Zr photoemission to provide a shift in energy appropriate for comparison of Zr spectral shapes.

Analysis of Zr 3p was performed using true Voigt line shapes formed via a convolution integral between Lorentzian and Gaussian functions. The relative width of the Gaussian with respect to the width of the Lorentzian is specified by the second parameter *b* in the line shape description LA(1,*b*) as defined by CasaXPS [12]. Bell shaped components representative of photoelectron intensity and satellite loss peaks are defined with respect to a Linear Shirley background defined by CasaXPS. A Linear Shirley background parameter

specifies a delay in the characteristic Shirley background shape, which for a standard Shirley background would occur directly below peak maxima. The use of the Linear Shirley background allows for a band gap expected for $ZrO_2$.

## Mapping XPS Photoemission Peak Position

Spectromicroscopy XPS data were acquired using stigmatic imaging of the analysis area. Signal was recorded with the material surface in a fixed position concerning the stage and stigmatic images were acquired over an energy interval using steps in energy between measurements equivalent to steps in energy performed during the measurement of spectra. Collection of such spectromicroscopy data is capable of creating large data sets and therefore requires special consideration compared to conventional spectroscopy data. The application of spectromicroscopy to understanding the effectiveness of charge compensation is subject to at least two problems that must be addressed to allow routine use of spectromicroscopy. First, collecting data sets of this nature is time-consuming and acquiring spectra at pixels in an unprocessed form with an appropriate signal to noise for understanding charge compensation would deter many from following the advice offered in this work. Similarly, large data sets making use of processing algorithms are limited by user tolerance for extended elapse times between initiating a procedure designed to recover spectral shapes and obtaining results. A solution to both these issues is presented here where an algorithm is described that permits shorter acquisition times by enhancing signal relative to noise and the algorithm is fast enough to prevent impatience for a solution deterring the use of these procedures. The effort, however, is the need for informed use of these techniques. The following is intended to provide insight into the algorithm to permit an informed use thereof.

## Singular Value Decomposition(SVD)

The basis for reducing acquisition times for spectromicroscopy is robust procedures for identifying and separating signals from noise. Singular Value Decomposition (SVD) has long been the basis for robust analysis of data sets into Principal Components (PCA) [13]. The approach described here makes use of iterative singular value decomposition (iSVD) [14] to perform two tasks that 1) permit the sorting of information within spectromicroscopy data sets [15] and 2) calculation of principal components characteristic of signal only. The temporal advantage of iSVD is achieved by sorting operations. The sorting of information allows the reduction in the size of the initial data set. An application of the transformations used throughout iSVD is used to collect a subset of images from the full data set, which possesses the essential information contained within the entire image set. Once a sufficiently reduce set of images is identified, the application of full precision iSVD to the subset of images generates a set of principal component abstract factors that can be used to reconstruct each image in the original data set. A consequence of these processing steps is spectra-at-pixels are created with spectral shapes from which an image is computed that

maps surface changes in apparent binding energy. Assuming a material surface is homogeneous in composition, charge compensation is assessed in terms of uniformity of potential by making use of these binding energy maps. The approach based on these maps used to understand charge compensation is one of the classifications of pixels with common binding energy from which spectra summed directly from raw data are used to demonstrate the range of possible shifts in energy over the analysis area.

The following is presented to provide a mathematical basis for the process applied to spectromicroscopy data used to enhance signal at the expense of noise. From an applications perspective, these signal enhancing steps are described as PCA, but from a mathematical perspective, PCA is implemented as the singular value decomposition of a matrix. The following expresses the essential features of SVD and the intimate relationship between PCA and linear least-squares approximations [16].

Given a matrix $\boldsymbol{Z}$ a singular value decomposition expresses $\boldsymbol{Z}$ in terms of three matrices $\boldsymbol{U}$, $\boldsymbol{V}$ and $\boldsymbol{W}$ as follows.

$$\boldsymbol{Z} = \boldsymbol{U}\boldsymbol{W}\boldsymbol{V}^T$$

These three matrices have the properties that $\boldsymbol{U}$ and $\boldsymbol{V}$ are orthogonal matrices ($\boldsymbol{V}^T\boldsymbol{V} = \boldsymbol{I}$ and $\boldsymbol{U}^T\boldsymbol{U} = \boldsymbol{I}$, $\boldsymbol{I}$ is the identity matrix) and $\boldsymbol{W}$ is a diagonal matrix. Such a decomposition of $\boldsymbol{Z}$ is useful for two reasons. Firstly the inverse matrix for $\boldsymbol{Z}$ is easily obtained as follows.

$$\boldsymbol{Z}^{-1} = \boldsymbol{V}\boldsymbol{W}^{-1}\boldsymbol{U}^T$$

The inverse $\boldsymbol{W}^{-1}$ is simply a diagonal matrix formed from the reciprocal of the diagonal elements of $\boldsymbol{W}$ and forming the transpose of a matrix is a simple matrix operation. Thus the only issue in finding the inverse matrix $\boldsymbol{Z}^{-1}$ can occur if diagonal elements of $\boldsymbol{W}$ are zero or close to zero in machine-precision terms. This observation leads to the second reason SVD is useful, namely, it is always possible to obtain a solution to a linear least-squares problem by SVD, even if the solution is of limited value.

The matrix $\boldsymbol{W}$ can be adjusted to allow a solution by avoiding division by zero that might occur when forming $\boldsymbol{W}^{-1}$. The problem of dividing by a number that is either zero or a number that contains sizeable loss of significant digits is accommodated by singular value decomposition by setting to zero problematic diagonal elements of $\boldsymbol{W}$. Setting troublesome elements of $\boldsymbol{W}$ to zero creates $\overline{\boldsymbol{W}}$ which implies the alternative matrix $\overline{\boldsymbol{Z}} = \boldsymbol{U}\overline{\boldsymbol{W}}\boldsymbol{V}^T$ that approximates the original matrix by projecting rows or columns of $\boldsymbol{Z}$ onto a subspace closest to the original subspace in the least-squares sense. This second point may not be intuitive to all, but by considering these concepts in three dimensions it is perhaps possible to visualize the essence of these ideas. The relationship to least squares can be visualized in terms of a three-dimensional vector and the relationship between the three-dimensional vector and a two-dimensional subspace (**Figure 1**).

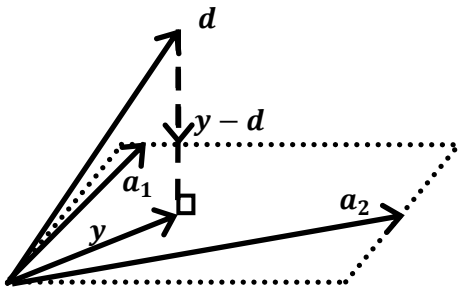


Figure 1: A vector $\boldsymbol{y} = c_1\boldsymbol{a_1} + c_2\boldsymbol{a_2}$ is a least-squares approximation to a vector $\boldsymbol{d}$ provided $\boldsymbol{y} - \boldsymbol{d}$ is parallel to the direction of the normal vector for the plane defined by vectors $\boldsymbol{a_1}$ and $\boldsymbol{a_2}$.

The logic for linear least-squares approximations depicted in **Figure 1** can be restated as follows. The vector $\boldsymbol{d}$ is expressed in terms of three vectors $\boldsymbol{a_1}$ , $\boldsymbol{a_2}$ and $\boldsymbol{a_3} = \boldsymbol{y} - \boldsymbol{d}$, where $\boldsymbol{a_3}$ is orthogonal to both $\boldsymbol{a_1}$ and $\boldsymbol{a_2}$**.** Assuming three coefficients are determined such that $\boldsymbol{d} = c_1\boldsymbol{a_1} + c_2\boldsymbol{a_2} + c_3\boldsymbol{a_3}$, the least-squares principle yields the approximation $\boldsymbol{y}$ to $\boldsymbol{d}$ by setting $c_3 = 0$.

SVD can be explained by analogy to the construction in **Figure 1**. SVD is an algorithm that accepts as input vectors $\boldsymbol{a_1}$ , $\boldsymbol{a_2}$ and $\boldsymbol{d}$, then returns three new vectors $\boldsymbol{u_1}$ , $\boldsymbol{u_2}$ and $\boldsymbol{u_3}$ that are mutually orthogonal and satisfy the following inequalities involving the vector cross product with corresponding unit vectors $\hat{\boldsymbol{u}}_1$ , $\hat{\boldsymbol{u}}_2$ and $\hat{\boldsymbol{u}}_3$.

[EQU SVD1] $$|\hat{\boldsymbol{u}}_1 \times \boldsymbol{a_1}|^2 + |\hat{\boldsymbol{u}}_1 \times \boldsymbol{a_2}|^2 + |\hat{\boldsymbol{u}}_1 \times \boldsymbol{d}|^2 \leq |\hat{\boldsymbol{u}}_2 \times \boldsymbol{a_1}|^2 + |\hat{\boldsymbol{u}}_2 \times \boldsymbol{a_2}|^2 + |\hat{\boldsymbol{u}}_2 \times \boldsymbol{d}|^2 \leq |\hat{\boldsymbol{u}}_3 \times \boldsymbol{a_1}|^2 + |\hat{\boldsymbol{u}}_3 \times \boldsymbol{a_2}|^2 + |\hat{\boldsymbol{u}}_3 \times \boldsymbol{d}|^2$$

Since $|\hat{\boldsymbol{u}} \times \boldsymbol{v}|^2$ is the square of the perpendicular distance between the position vector $\boldsymbol{v}$ and a line in the direction of $\hat{\boldsymbol{u}}$ through the origin (**Figure 2**), the least-squares principle underlies the construction steps leading to an SVD in the following sense.

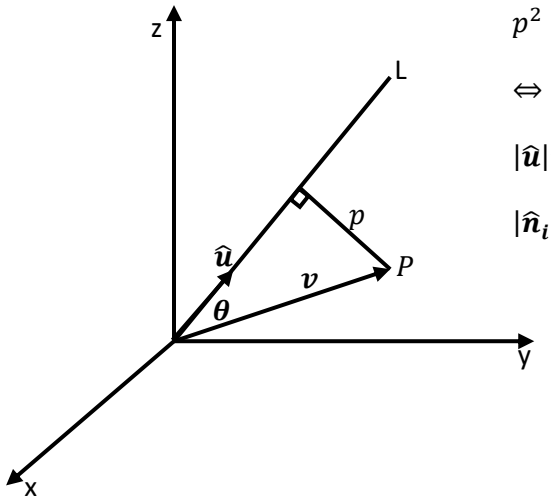


$$p^2 = |\hat{\boldsymbol{u}} \times \boldsymbol{v}|^2$$

$$\Leftrightarrow p^2 = (|\hat{\boldsymbol{u}}||\boldsymbol{v}|sin\theta\hat{\boldsymbol{n}}_{\boldsymbol{i}}).(|\hat{\boldsymbol{u}}||\boldsymbol{v}|sin\theta\hat{\boldsymbol{n}}_{\boldsymbol{i}})$$

$$|\hat{\boldsymbol{u}}|^2 = 1$$

$$|\hat{\boldsymbol{n}}_{\boldsymbol{i}}|^2 = 1$$

Figure 2: Perpendicular distance $p$ of a point P in 3D space to a line L in the direction of the unit vector $\hat{\boldsymbol{u}}$. If $\boldsymbol{v}$ is a position vector to the point P then the perpendicular distance is computed using the vector cross product. The line L approximating a set of points in 3D is obtained by minimizing the sum of square distances calculated for the set of points. If three vectors $\boldsymbol{a_1}$, $\boldsymbol{a_2}$ and $\boldsymbol{d}$ define three points in 3D, then the process of computing $\hat{\boldsymbol{u}}_{\boldsymbol{1}}$ as a step in SVD is the same as minimizing the sum of square distances defined in Equation SVD1.

Given these SVD vectors $\boldsymbol{u_1}$ , $\boldsymbol{u_2}$ and $\boldsymbol{u_3}$ then expressing $\boldsymbol{d}$ in the form $\boldsymbol{d} = b_1\boldsymbol{u_1} + b_2\boldsymbol{u_2} + b_3\boldsymbol{u_3}$ is an equivalent statement to $\boldsymbol{d} = c_1\boldsymbol{a_1} + c_2\boldsymbol{a_2} + c_3\boldsymbol{a_3}$ with the difference that, if as part of the SVD calculation the vector $\boldsymbol{u_3}$ is associated with an element of $\boldsymbol{W}$ that is set to zero, then the SVD solution results in $\boldsymbol{d} \cong b_1\boldsymbol{u_1} + b_2\boldsymbol{u_2}$. Thus setting an element of $\boldsymbol{W}$ to zero conforms to a least-squares principle by projecting $\boldsymbol{d}$ onto the plane defined by the vectors $\boldsymbol{u_1}$ and $\boldsymbol{u_2}$. Setting an element of $\boldsymbol{W}$ to zero occurs whenever the calculation encounters a problem inverting the matrix $\boldsymbol{Z}$ as a result of attempting to compute the coefficient $b_3$. Hence the least-squares principle is applied in computing precise SVD results and the fix for imprecise results is to invoke a least-squares principle.

While it is clear, perhaps, that mathematically SVD is a remarkably useful concept, however, how to compute SVD for a matrix is not so clear. There are several approaches to computing SVD for a matrix which include techniques for computing partial SVD. That is if the intention is to obtain a least-squares solution that involves neglecting a proportion of the calculated matrices there is little point in expending time on calculations that will be ignored. Some algorithms such as NIPALS specifically target the first few columns of $\boldsymbol{U}$ and $\boldsymbol{V}$, but others require all columns to be computed before discarding columns to satisfy the requirements for a solution. The approach adopted in CasaXPS software is iterative SVD which is capable of both targeting a limited number of columns in $\boldsymbol{U}$ and $\boldsymbol{V}$, and also, when required, computing all columns of $\boldsymbol{U}$ and $\boldsymbol{V}$ together with $\boldsymbol{W}$ to machine precision.

While a discussion based on three-dimensional vectors may seem remote to a discussion aimed at vectors formed from images, the link between these two concepts is obtained by observing SVD applied to three data vectors $\{ \boldsymbol{d}_1, \boldsymbol{d}_2, \boldsymbol{d}_3 \}$, where $\boldsymbol{d}_i \in \mathbb{R}^n$ and $n$ equals the number of pixels in an image, is as simple as computing a 3x3 covariance matrix for a data matrix $\boldsymbol{D_3} = [\, \boldsymbol{d}_1, \boldsymbol{d}_2, \boldsymbol{d}_3 \,]$

$$\boldsymbol{Z_3} = \boldsymbol{D_3}^T \boldsymbol{D_3}$$

or

$$\boldsymbol{Z_3} = \begin{bmatrix} \boldsymbol{d}_1.\boldsymbol{d}_1 & \boldsymbol{d}_1.\boldsymbol{d}_2 & \boldsymbol{d}_1.\boldsymbol{d}_3 \\ \boldsymbol{d}_1.\boldsymbol{d}_2 & \boldsymbol{d}_2.\boldsymbol{d}_2 & \boldsymbol{d}_2.\boldsymbol{d}_3 \\ \boldsymbol{d}_1.\boldsymbol{d}_3 & \boldsymbol{d}_2.\boldsymbol{d}_3 & \boldsymbol{d}_3.\boldsymbol{d}_3 \end{bmatrix}$$

Computing the eigenvectors for $\boldsymbol{Z_3}$ creates a set of vectors $\boldsymbol{U} = [\hat{\boldsymbol{u}}_1, \hat{\boldsymbol{u}}_2, \hat{\boldsymbol{u}}_3]$, where $\boldsymbol{u}_i \in \mathbb{R}^n$, satisfying the conditional relationship EQU SVD1. Indeed, the eigenvector equation for the covariance matrix is derived by calculus to impose the conditional relationship EQU SVD1. The critical point to observe is these three vectors can be ordered by the magnitude of eigenvalues to achieve the inequalities in EQU SVD1. Effectively these new vectors have a natural ordering that permits the movement of vectors within the data set based on eigenanalysis for three vectors at a time and it is in this sense that SVD sorts information content in data vectors.

When the number of data vectors is $m \geq 3$ iterative SVD is performed to obtain the SVD for $m$ data vectors $\boldsymbol{D_m} = \left[\boldsymbol{d}_1, \boldsymbol{d}_2, \boldsymbol{d}_{3,} \cdots, \boldsymbol{d}_m\right]$ by an iterative scheme computing one eigenvalue and corresponding eigenvector at a time.

initialize a set of vectors $\boldsymbol{y}_1, \boldsymbol{y}_2, \boldsymbol{y}_{3,} \cdots, \boldsymbol{y}_m$ equal to the set of data vectors $\boldsymbol{d}_1, \boldsymbol{d}_2, \boldsymbol{d}_{3,} \cdots, \boldsymbol{d}_m$

repeat “while current approximation to largest eigenvector has not converged”

loop $i = m$ down to 3 do

“replace the vectors $\boldsymbol{y}_1$, $\boldsymbol{y}_2$ and $\boldsymbol{y}_i$ by transformed vectors corresponding to the eigenvectors of covariance matrix computed from $\boldsymbol{y}_1$, $\boldsymbol{y}_2$ and $\boldsymbol{y}_i$ in the order of magnitude of the eigenvalues and return the largest eigenvalue.”

on exit $\boldsymbol{u_1} = \boldsymbol{y}_1$

The success of iterative SVD is due to the generalization of a Jacobi rotation performed as part of the Jacobi algorithm that determines eigenvectors for a real symmetric matrix [16]. The covariance matrix $\boldsymbol{Z_m}$ is a real symmetric matrix. A Jacobi rotation is simply a matrix operation computed from two vectors at a time that is mathematically equivalent to determining the eigenvectors for a 2x2 covariance matrix. Iterative SVD extends the Jacobi rotation from 2x2 to 3x3 by performing a transformation of a real symmetric matrix

analogous to a Jacobi rotation, but zeros six matrix elements per transformation rather than zeroing only two elements achieved per Jacobi rotation.

## Results and discussion

### The basis for the inaccuracies of $ZrO_2$ spectral envelopes obtained using XPS

High-resolution Zr 3d and O 1s spectra are shown in **Figure 3**. The Shirley algorithm applied to data from a sample with a sizeable bandgap is one source for error in measured peak intensity [17,18]. While a Shirley-type response of inelastically scattered electrons to a sample without an appreciable band gap has some merit, a material with a bandgap means that there is threshold energy below which energy loss is unlikely. In the case of $ZrO_2$, by considering the background associated with O 1s it can be inferred photoemission signal when inelastic scattering occurs creates background signal offset in energy from electrons recorded without energy loss. A Shirley background computed in the most basic form applied to Zr photoemission from $ZrO_2$ raises the background prematurely (reducing the measured peak area) compared to a background that delays the Shirley step and hence a basic Shirley background is a poor approximation to the true background beneath Zr photoemission peaks. Relative sensitivity factors used to compare photoemission peak intensity reduces the consequences of using a basic Shirley background when comparing Zr photoemission only. However, since the O 1s photoemission background from $ZrO_2$ is flat no step occurs in the background computed via the basic Shirley algorithm, therefore the cost of using a basic Shirley background is felt the most when comparing Zr photoemission to O 1s photoemission.

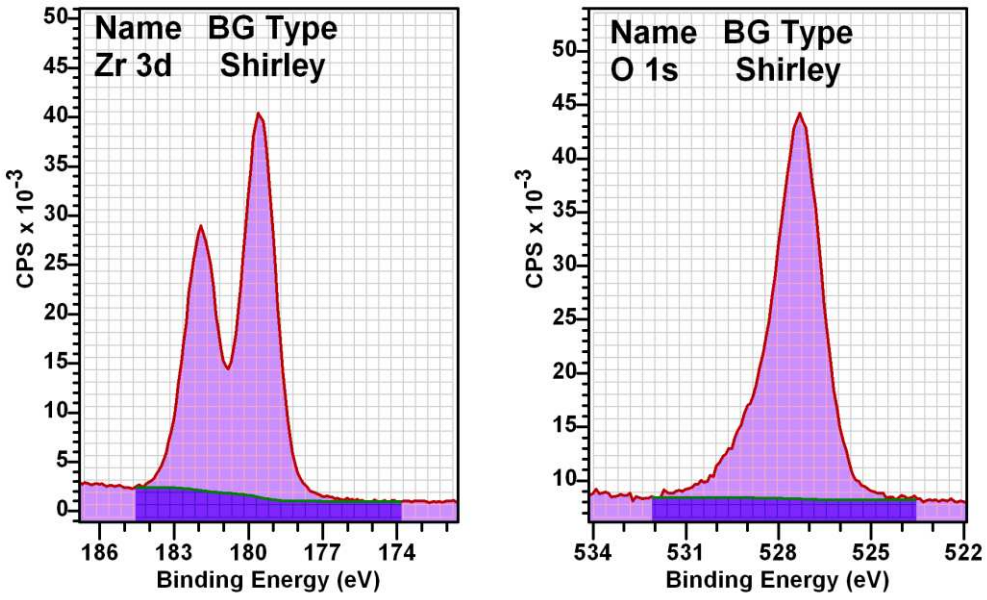


Figure 3: (Right) O 1s spectrum measured from $ZrO_2$. Evidence that supports a wide bandgap of about 6 eV is the flat response of background intensity beneath the O 1s photoemission peak. (Left) A basic Shirley background computed from data applied to Zr 3d photoemission.

When estimating photoemission intensity from Zr 3p a second source for error is introduced by ignoring resonant shapes in the background signal. The evidence for interference from loss peaks with Zr 3p is the background shapes associated with Zr 3d. The importance of correctly accounting for loss peaks can be seen by considering how a region might be defined for Zr 3p and Zr 3d. A loss peak obvious and separate from Zr 3d is located at about 13 eV to lower kinetic energy than the Zr 3d doublet (see **Figure 5**). A region defined for Zr 3d would typically extend over an interval that did not include the loss structure. Assuming similar loss structures are associated with Zr 3p, then Zr $3p_{3/2}$ would be responsible for a loss structure located in energy close to Zr $3p_{1/2}$. The existence of a loss structure beneath Zr $3p_{1/2}$ is supported by calculating the ratio of Zr $3p_{1/2}$ to Zr $3p_{3/2}$. The expected ratio for these two peaks forming the Zr 3p doublet should be close to the ratio 1:2, which is not the case for Zr 3p. Hence a region defined over an interval including both doublet peaks of Zr 3p would not be equivalent to the region defined for Zr 3d.

## Further interpretation of spectroscopic $ZrO_2$ data

The stability of spectra concerning repeat measurements demonstrates steady-state charge compensation has been achieved. These same repetitious spectra also demonstrate the sample is not changing chemistry with time. The assumption regarding this latter statement is that the lack of energy shifts or changes in peak shapes implies an element is unchanged in chemical character. Hence the first experiment involved measuring the sample multiple times in spectroscopic mode. The survey data shown in **Figure 4** are two spectra measured sequentially from the same location on the $ZrO_2$ sample in the same area. These spectra demonstrate the repeatable nature of photoemission peaks measured at either extreme of the energy range. Comparing these two survey spectra support an assertion that, with the aid of charge compensation, $ZrO_2$ powder on carbon tape attains a steady-state potential.

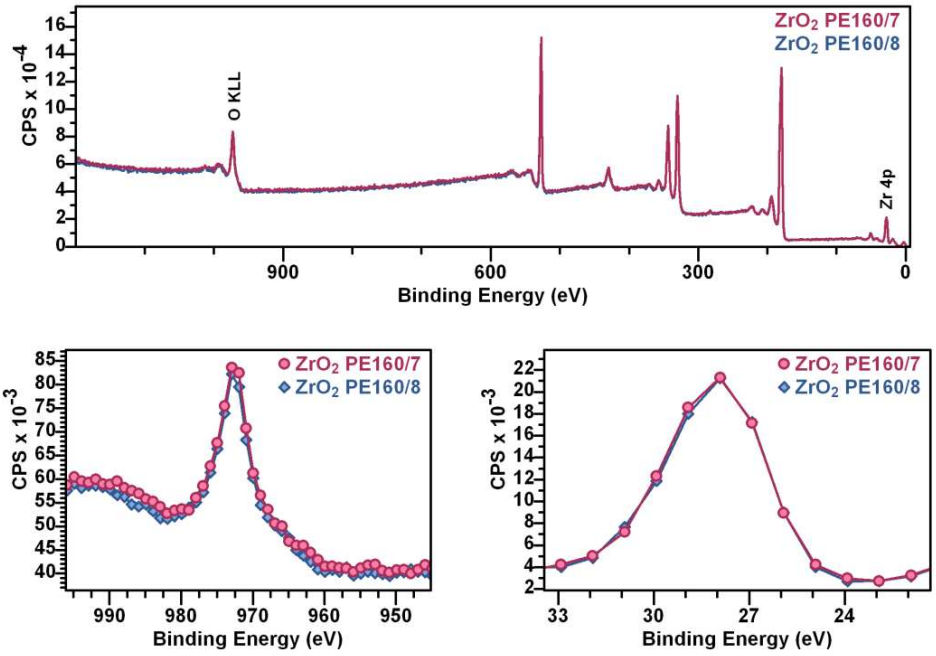

Figure 4: Comparison of two survey spectra (Hybrid lens mode pass energy 160) showing the stability of peak position between these two measurements. If the sample failed to arrive at a steady-state (for electrons emitted from the sample and electrons returned to the sample by charge compensation) then the relative position of photoemission peaks would evolve with time.

The anomaly described for Zr 3p doublet peak intensities was further examined using narrow scan data. Spectra measured over a narrow energy interval allow a smaller step size than is typical of survey-type data and the dwell-time can be tailored to the sensitivity of a particular photoemission peak. Narrow scan spectra for O 1s, Zr 3p, Zr 3d, Zr 4s and Zr 4p are acquired using Hybrid lens mode operating at pass energy 40 eV. These narrow scan spectra are used to 1) demonstrate the stability of spectral shapes concerning time and 2) verify the stability of sample chemistry concerning the measurement process. Thirty-two spectra were measured per narrow scan for a given photoemission peak. After charge correction based on Zr $3d_{5/2}$, these four narrow scan spectral regions are displayed overlaid in **Figure 5**. The stability of these spectra is evidenced by plotting three Principal Component Analysis (PCA) abstract-factors per narrow-scan interval in **Figure 6**. These abstract factors are the second, third and fourth abstract factors and, for the most part, show no significant structure other than variations about peak maxima which is expected for Poisson distributed noise. The exception is O 1s data where the second abstract factor includes evidence of alterations in O 1s peak shape or energy, but all zirconium photoemission suggests little change in spectral form during these experiments.

Results shown in **Figure 5** and **Figure 6** rely on applying an offset in energy for individual measurements for each narrow scan based on aligning Zr 3d peak maxima. The assumption when making such adjustments to the energy scale is the sample (during exposure to X-rays and charge compensation) has achieved a balance of potential at the surface. While these results are encouraging, there is still the possibility these data are measured from a sample in a steady-state, but a steady-state that may include zones within the analysis area for which different potentials are nevertheless present.

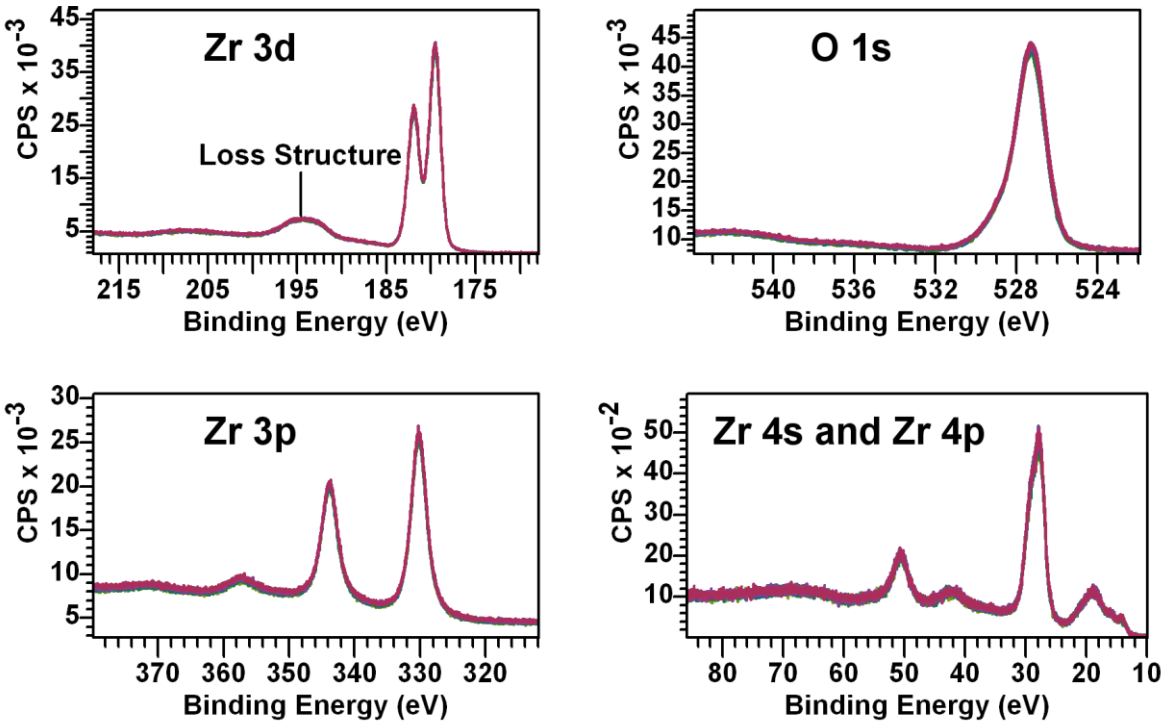


Figure 5: Narrow scan spectra measured from the same location on the sample. These data are all shifted in energy by an offset determined from Zr $3d_{3/2}$ to align the maximum intensity defined by fitting two components to the data shown in the display tile labeled Zr 3d.

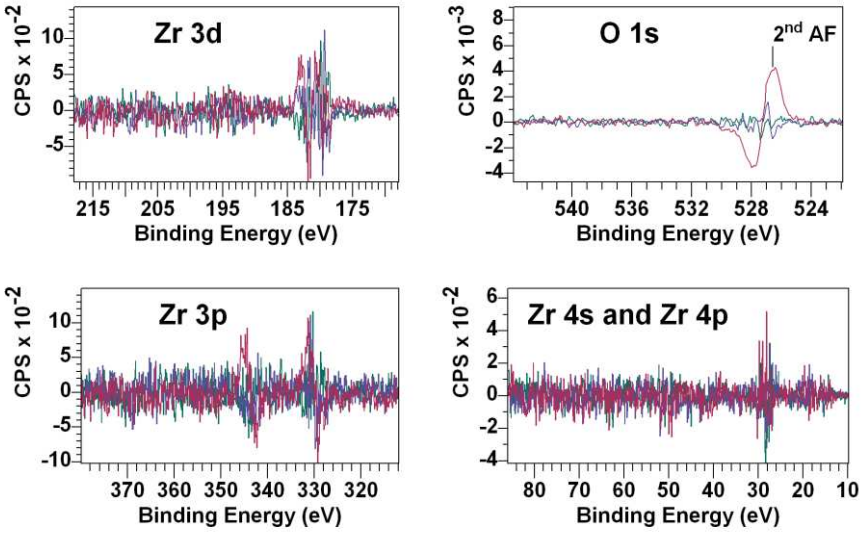


Figure 6: Principal Component Analysis (PCA) of data in Figure 5 yields a set of abstract factors for each narrow scan spectra. The first and most significant abstract factor in each case is a shape similar to the shape obtained by averaging of spectra over 32 spectra per narrow scan. Higher abstract factors are a measure for the deviation from the shape

obtained for the first abstract factor. These display tiles show three abstract factors, ordered by significance, omitting the first and most significant abstract factor. These plots for each Zr photoemission state show variations consistent with Zr spectra that are essentially identical in shape and position. Small increases in oscillations correspond to peak maxima and are consistent with data containing noise varying as the square root of counts per bin.

## Analysis of spectromicroscopy data of $ZrO_2$ surfaces

The success of charge compensation assessed purely based on spectroscopic evidence is open to question. Charge correction based on aligning C 1s line at 284.8 eV is also questionable [2,3,19,20]. This is particularly true for spectra with peaks of significant width or shapes formed from chemically shifted component peaks. Information about the interaction of a charge compensation mechanism and particular material surfaces is in this work obtained via measuring spectromicroscopy data sets based on a particular photoemission line. In particular, images were collected using steps in energy over an interval corresponding to Zr 3d with the objective for an imaging experiment applied to a powder such as $ZrO_2$ to verify spectra calculated from image pixels are identical over the analysis area. Ultimately, these images measured from a powder should be uniform. The signal to noise for data measured using spatially resolved XPS tends to be low compared to spectra collected using multiple energy channels in parallel, hence the processing of image data is an important step in understanding spectra gathered from image data sets. Processing of image data may be as simple as grouping pixels geometrically or creating a grouping of pixels using assigning false colors to pixels based on intensity or other criteria. PCA-based noise reduction is necessary when deriving spectra at pixels suitable for measuring the variation of position or FWHM, for example. **Figure 7** presents results obtained from images measured over an energy interval corresponding to Zr 3d where pixel values are gathered from the binding energy recorded for each spectrum-at-pixels peak maximum of Zr $3d_{5/2}$. Colors in the processed image, therefore, reflect energy differences over the analysis area defined by the field of view 650 $um^2$. Once a binding energy map is obtained, spectra integrated from pixels with identical colors similarly demonstrate shifts in the energy of less than 0.3 eV. The depth of the valley between the doublet peaks for Zr 3d is an indication of energy resolution.

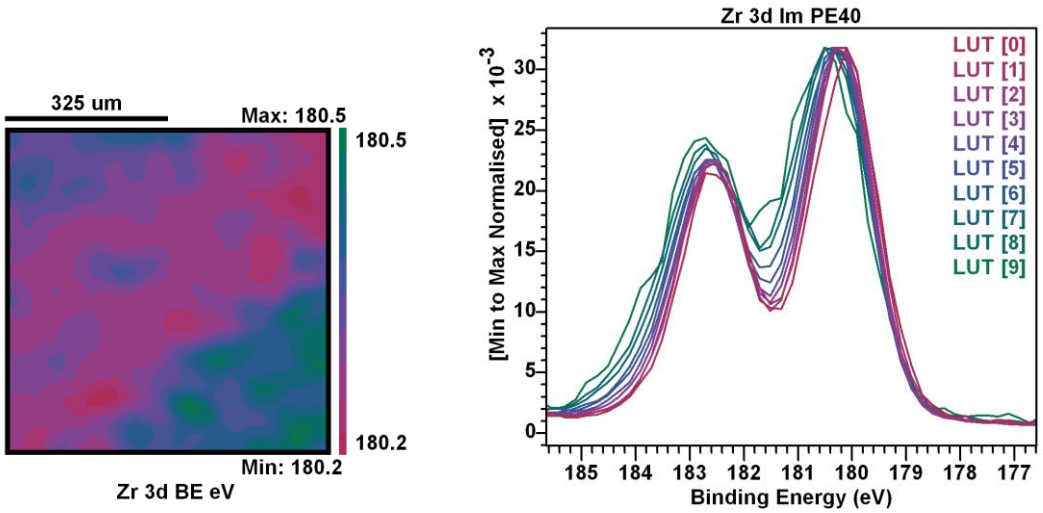


Figure 7: An image formed from Zr 3d spectra-at-pixels is partitioned in binding energy (BE) using a false-color scale from which integrated spectra-at-pixels result in a ten look-up table (LUT) spectra. The color scale used to display pixel colors spans binding energies between 180.2 and 180.5 eV. Shifts in Zr $3d_{5/2}$ seen in integrated spectra reflect the color variation in the image.

Energy shifts of the nature shown in **Figure 7** may result from several reasons. One reason might be a variation of photon energy with position over the field of view. Another may be localized variation in the efficiency of charge compensation. Regardless of the reason for these shifts, these spectra gathered from a spectromicroscopy data set suggest the material surface is behaving reasonably well given the nature of the material surface and the limitations of stigmatic imaging. Specifically, Zr 3d spectra measured directly from the material surface (**Figure 6**) using PE 40 compare favorably with the best energy resolution spectra measured indirectly by imaging (**Figure 7**). The evidence suggests investigating the relative intensities for doublet peaks due to Zr 3p based on these measurements is appropriate.

## Peak model for Zr 3p in $ZrO_2$

When fitting Zr 3p, the correct ratio for two peaks forming the doublet is obtained only if a component in the peak model accounts for a loss structure present in Zr 3d photoemission (**Figure 8**).

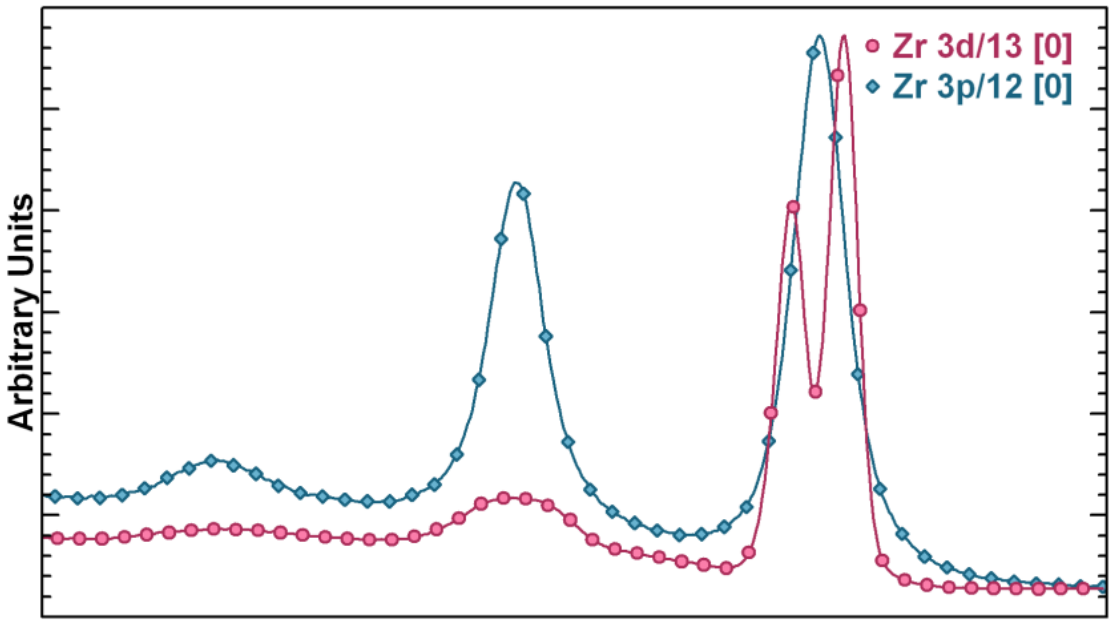


Figure 8: Comparison of Zr 3d and Zr 3p illustrating the influence of background loss structures obvious for Zr 3d that must also play a role for Zr 3p photoemission. Specifically, a loss peak shape due to Zr $3p_{3/2}$ coincides with Zr $3p_{1/2}$. These data are collected using conventional spectroscopy with pass energy 40. In particular, Zr 3d data shown here are comparable to Zr 3d shown in **Figure 7**.

The peak model in **Figure 9** illustrates features of Zr 3p that not only correspond to loss structures but also allows for inelastic scattering via the use of an offset in energy applied to the sigmoid Shirley shape in a background approximation. Such an offset in the onset of a Shirley response to a photoemission peak is justified based on a significant bandgap associated with $ZrO_2$.

A test for the peak model shown in **Figure 9** is the application of the peak model to 32 similar spectra measure from the same material surface (**Figure 10**). If a peak model is well-formed then the response of fitting the peak model when fit to different spectra should be small variations for each component concerning all spectra used in the test. **Figure 10** suggests the peak model is robust in the sense that after optimization applied to equivalent spectra the outcomes are independent of the spectrum to which the model is applied.

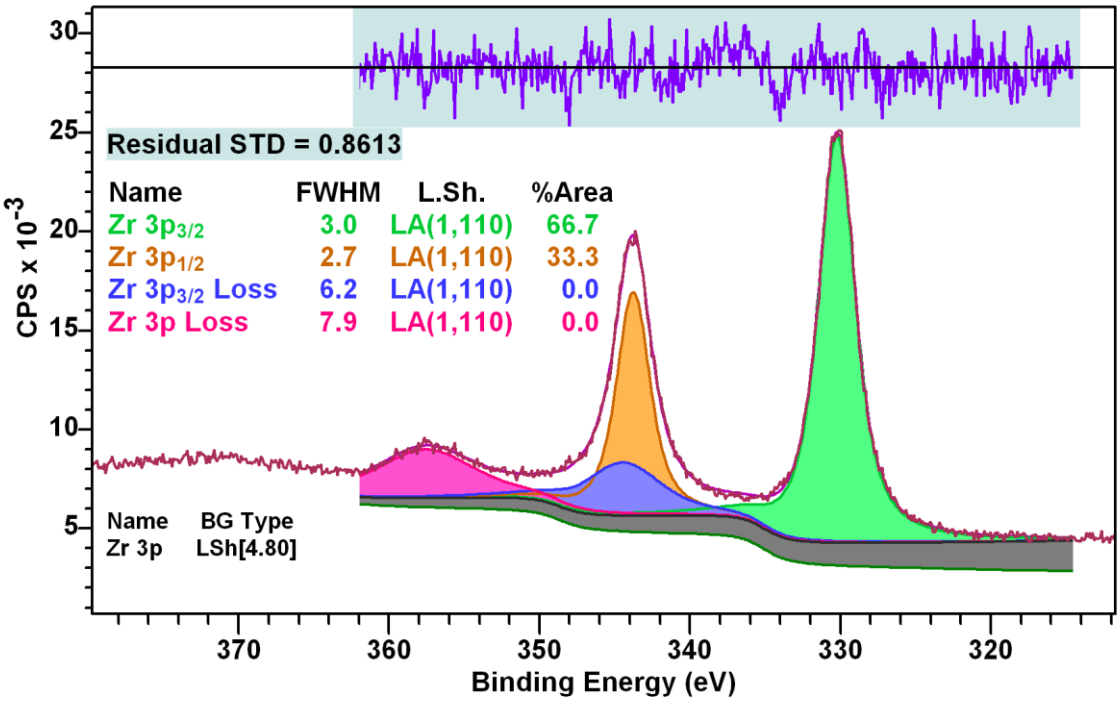


Figure 9: Peak model for Zr 3p doublet where the predicted ratio for Zr $3p_{1/2}$ to Zr $3p_{3/2}$ is obtained only when a loss component corresponding to Zr $3p_{3/2}$ is included beneath signal corresponding to Zr $3p_{1/2}$.

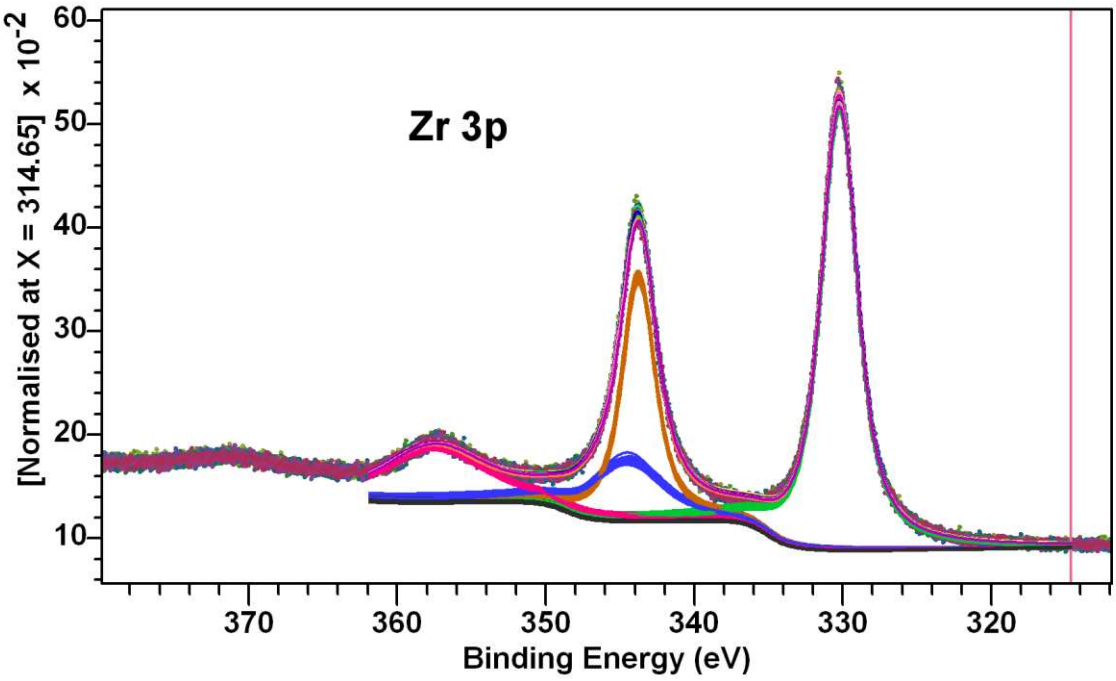


Figure 10: Variation of peak model results when applied to 32 spectra measured from the same material surface of $ZrO_2$.

The conclusion from the analysis of Zr 3p is that even apparently simple doublet spectra require careful consideration and the most obvious approach to fitting such data is not always the most appropriate. Placing Zr 3p spectra in the context of other photoemission peaks is essential when constructing a more physically meaningful peak model for Zr 3p.

## Application of verification procedures to complex $ZrO_2$ supported materials

The material surface considered up to this point is expected to be homogeneous $ZrO_2$. The peak model in **Figure 9** demonstrates little other than the types of shapes that are possible with Zr 3p. However, such a peak model becomes useful when considering $ZrO_2$ containing different proportions of palladium. For small amounts of palladium in a predominantly $ZrO_2$ material surface requires the analysis of the same energy interval involving component peaks representative of Pd 3d and Zr 3p. Without appreciating the loss structures due to Zr $3p_{3/2}$ it would be easy to overestimate the amount of palladium in a material surface and/or misinterpret the chemical state for palladium. There is one further danger to an analysis of material surfaces including Zr and Pd, namely, if for any reason a material surface responded badly to charge compensation, for small proportions of Pd in a material surface, charge shifted Zr 3p could prevent a clear understanding of Pd 3d. Verification of a material surface's response to charge compensation is therefore significant to the study of catalysts.

A $ZrO_2$ material surface prepared with palladium 10% by weight is measured using the protocol described in Materials and methods. Mapping the energy of Zr $3p_{3/2}$ demonstrates a systematic shift in binding energy from bottom-left to top-right of the imaged area (**Figure 11 top-left**). The maximum shift identified by spectromicroscopy is 0.3 eV. Shifts of this nature are possibly due to instrumental factors. The systematic shift within this energy range is observed for silver material surfaces measure by stigmatic imaging on a Kratos Axis Ultra [21]. Therefore, the results shown in **Figure 11** support the use of these data to assess the relationship of Pd to Zr using peak fitting.

The peak model is shown in **Figure 11 (bottom-right)** is prepared for data collected in spectroscopic mode. Spectroscopic mode on a Kratos Axis Ultra makes use of an analysis area defined by the slot selected area aperture that limits recorded photoelectrons to *ca.* 300x700 $\mu m^2$ which is a proportion of the imaged area shown in **Figure 11 (top-left)**. The spectrum in the bottom-left panel is computed from spectromicroscopy data. All pixels within the spectromicroscopy data set are used to compute a spectrum by utilizing the spectra shown in **Figure 11 top-right** after aligning Zr $3p_{3/2}$ component peaks followed by the summation of energy-adjusted spectra to form the spectrum in the bottom-left panel. The same peak model applied to the spectrum computed from spectromicroscopy and the spectrum measured in spectroscopy mode shows consistency of outcome. Note that the quality of fit for spectromicroscopy data is best judged by the residual plot. These data in **Figure 11 bottom-left** were acquired in a mode that modified raw counts per bin, therefore the residual standard deviation is about five times larger than expected. Hence the evidence

from spectromicroscopy data in **Figure 11** supports the use of a peak model in **Figure 11 bottom** to interpret signal in terms of Pd and Zr.

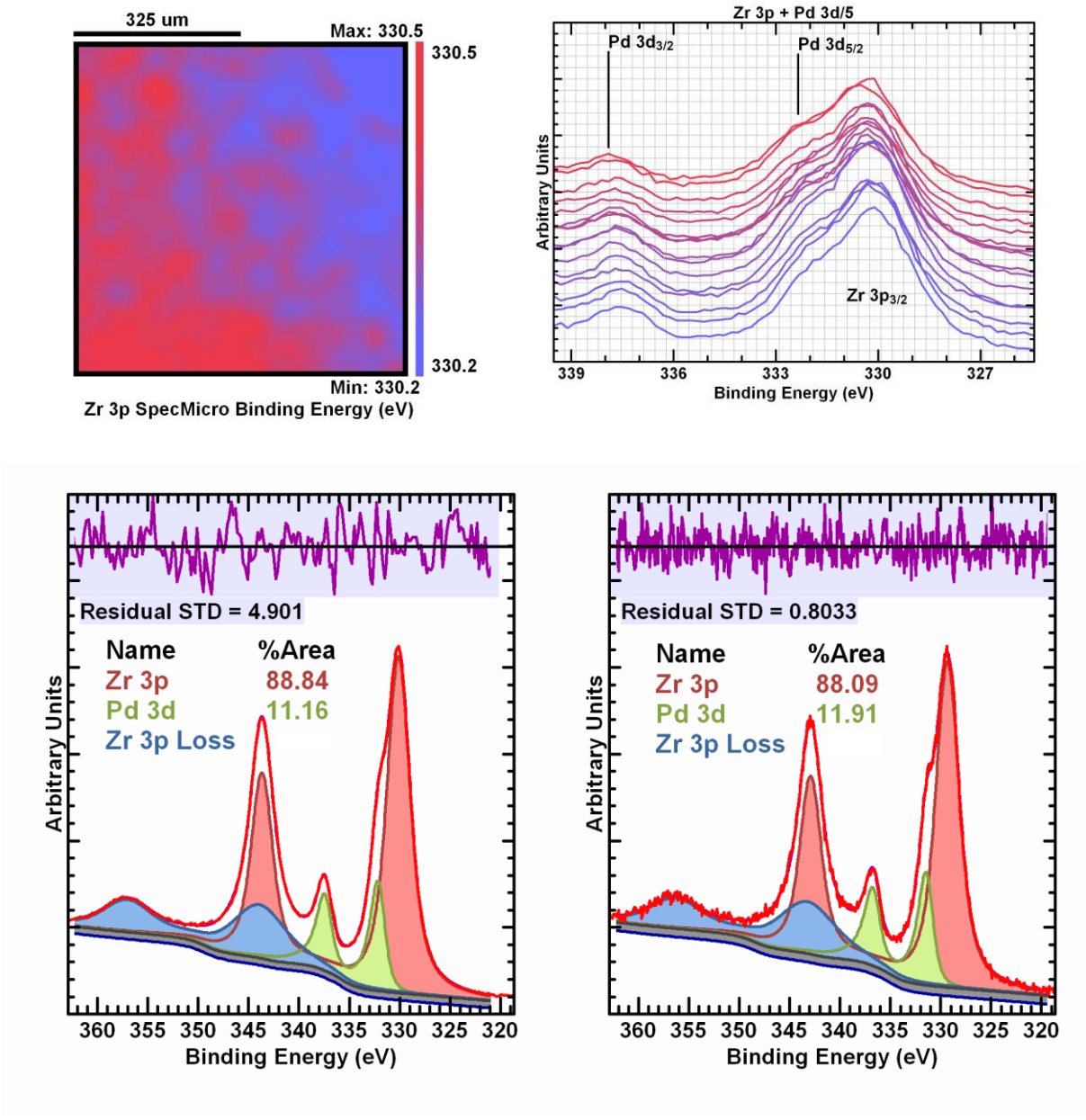


Figure 11: Top-left: Surface of Zr/Pd material surface mapped in terms of peak position for Zr $3p_{3/2}$. Top-right: Spectra calculated from spectromicroscopy data set corresponding to pixel classification by color shown in the top-left image. Bottom-left: Spectromicroscopy spectrum computed from data shown in Top-right panel by aligning LUT spectra in energy concerning Zr $3p_{3/2}$ component before summing to form the total spectrum. Bottom-right: $ZrO_2$/Pd material surface analyzed by peak model applied to spectroscopic data following verification of data quality using spectromicroscopy.

On the evidence of data shown so far one might conclude these analyses are academic as a positive outcome appears typical. Unfortunately, charge compensation interactions with material surfaces of different compositions, structure and conductivity may not behave as well as these examples involving $ZrO_2$. **Figure 12** is an example of a material surface that responded to charge compensation by creating a steady-state potential but unfortunately, the potential at each point on the material surface is not uniform. A map of the position for N 1s photoemission shown in **Figure 12** illustrates the cause of the problem.

However, for this case, the magnitude of these shifts is such that an issue would be recognized in spectroscopic data. A greater problem occurs when changes in potential across the analysis area are less severe and therefore less obvious in spectra. Under these more subtle situations, the importance of chemical state analysis of spectromicroscopy is more apparent.

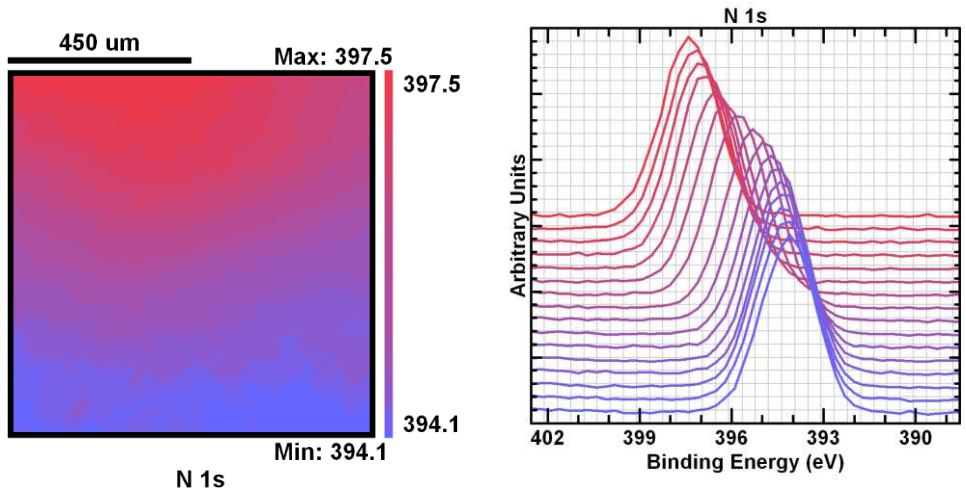


Figure 12: An example of failure for charge compensation. The sample and charge compensation failed to create a uniform steady state potential for the sample. Problems easily demonstrated by mapping the surface in terms of peak binding energy are so server that these would be recognised in spectroscopic data without too much trouble. A greater issue occurs where shifts of this nature occur but not to the same extent and therefore are difficult to detect without spectromicroscopy.

## Conclusions

The application of spectromicroscopy to understanding the effectiveness of charge compensation is subject to at least two problems that must be addressed to allow routine use of spectromicroscopy. First, collecting data sets of this nature is time-consuming and acquiring spectra at pixels in an unprocessed form with an appropriate signal to noise for understanding charge compensation would deter many from following the advice offered in this paper. Similarly, for large data sets making use of processing algorithms is limited by user tolerance for extended elapse times between initiating a procedure designed to recover spectral shapes and obtaining results. A solution to both these issues is developed

here where an algorithm is described that permits shorter acquisition times by enhancing signal relative to noise and the algorithm is fast enough to prevent impatience for a solution deterring the use of these procedures. The cost however is the need for informed use of these techniques. The following is intended to provide insight into the algorithm to permit an informed use thereof.

The examples presented in this paper illustrate how XPS imaging, coupled with techniques for enhancing signal in spectromicroscopy data, allows chemical state analysis of conventional spectroscopic data with confidence that shapes, in spectra, are without artifacts due to charge compensation. While spectroscopy remains the focus of many papers containing XPS data, chemical state interpretation of spectra measured from insulating materials is always open to criticism relating to charge compensation. While far fewer papers address scientific problems using XPS imaging, an important role for XPS imaging is in supporting outcomes presented from spectra, particularly where charge compensation may be less than perfect. This paper demonstrates how spectromicroscopy can be used to allay such doubts.

## Acknowledgments

This work was supported as part of the Center for Understanding and Control of Acid Gas-Induced Evolution of Materials for Energy (UNCAGE-ME), an Energy Frontier Research Center funded by the U.S. Department of Energy, Office of Science, Basic Energy Sciences under Award No. DE-SC0012577. The CNRS is acknowledged for financial support to the Thematic Workshop (N° 1317144) held at the Station Biologique, Roscoff, France.

## CRediT author statement

**Pascal Philippe Bargiela**: Investigation (lead); Conceptualization (supporting). **Vincent Fernande**z: Investigation (supporting). **Christophe Cardinaud**: Investigation (supporting). **John Walton**: writing – review and editing (equal); Methodology (supporting). **Mark Greiner**: writing – review and editing (equal); Methodology (supporting). **David Morgan**: writing – review and editing (equal); Methodology (supporting). **Neal Fairley**: Methodology (lead); Conceptualization (lead); Writing – original draft (equal); writing – review and editing (equal). **Jonas Baltrusaitis**: Conceptualization (supporting); Methodology (supporting) Funding acquisition; Writing – original draft (equal); writing – review and editing (equal).

## References


[1] D.R. Baer, K. Artyushkova, C. Richard Brundle, J.E. Castle, M.H. Engelhard, K.J. Gaskell, J.T. Grant, R.T. Haasch, M.R. Linford, C.J. Powell, A.G. Shard, P.M.A. Sherwood, V.S. Smentkowski, Practical guides for x-ray photoelectron spectroscopy: First steps in planning, conducting, and reporting XPS measurements, J. Vac. Sci. Technol. A. 37 (2019) 031401. https://doi.org/10.1116/1.5065501.

[2] D.R. Baer, K. Artyushkova, H. Cohen, C.D. Easton, M. Engelhard, T.R. Gengenbach, G. Greczynski, P. Mack, D.J. Morgan, A. Roberts, XPS guide: Charge neutralization and binding energy referencing for insulating samples, J. Vac. Sci. Technol. A. 38 (2020) 031204. https://doi.org/10.1116/6.0000057.

[3] G. Greczynski, L. Hultman, X-ray photoelectron spectroscopy: Towards reliable binding energy referencing, Prog. Mater. Sci. 107 (2020) 100591. https://doi.org/10.1016/j.pmatsci.2019.100591.

[4] H. Jiang, R.I. Gomez-Abal, P. Rinke, M. Scheffler, Electronic band structure of zirconia and hafnia polymorphs from the GW perspective, Phys. Rev. B. 81 (2010) 085119. https://doi.org/10.1103/PhysRevB.81.085119.

[5] K. Tomishige, Y. Ikeda, T. Sakaihori, K. Fujimoto, Catalytic properties and structure of zirconia catalysts for direct synthesis of dimethyl carbonate from methanol and carbon dioxide, J. Catal. 192 (2000) 355–362. https://doi.org/https://doi.org/10.1006/jcat.2000.2854.

[6] Y. Wu, J. Chen, W. Hu, K. Zhao, P. Qu, P. Shen, M. Zhao, L. Zhong, Y. Chen, Phase transformation and oxygen vacancies in Pd/ZrO2 for complete methane oxidation under lean conditions, J. Catal. 377 (2019) 565–576. https://doi.org/https://doi.org/10.1016/j.jcat.2019.04.047.

[7] W.S. Epling, G.B. Hoflund, Catalytic Oxidation of Methane over ZrO2-Supported Pd Catalysts, J. Catal. 182 (1999) 5–12. https://doi.org/https://doi.org/10.1006/jcat.1998.2341.

[8] J.-H. Park, J.H. Cho, Y.J. Kim, E.S. Kim, H.S. Han, C.-H. Shin, Hydrothermal stability of Pd/ZrO2 catalysts for high temperature methane combustion, Appl. Catal. B Environ. 160–161 (2014) 135–143. https://doi.org/https://doi.org/10.1016/j.apcatb.2014.05.013.

[9] D. Ruano, B.M. Pabón, C. Azenha, C. Mateos-Pedrero, A. Mendes, V. Pérez-Dieste, P. Concepción, Influence of the ZrO2 Crystalline Phases on the Nature of Active Sites in PdCu/ZrO2 Catalysts for the Methanol Steam Reforming Reaction—An In Situ Spectroscopic Study, Catal. . 10 (2020). https://doi.org/10.3390/catal10091005.

[10] K.N. Patil, D. Prasad, J.T. Bhanushali, B. Kakade, A.H. Jadhav, B.M. Nagaraja, Chemoselective hydrogenation of cinnamaldehyde over a tailored oxygen-vacancy-rich Pd@ZrO2 catalyst, New J. Chem. 45 (2021) 5659–5681. https://doi.org/10.1039/D0NJ05595F.

[11] D.A. Shirley, High-Resolution X-Ray Photoemission Spectrum of the Valence Bands of

Gold, Phys. Rev. B. 5 (1972) 4709–4714. https://doi.org/10.1103/PhysRevB.5.4709.

[12] N. Fairley, V. Fernandez, M.R.C. Guillot-Deudonn, J. Walton, E. Smith, D. Flahaut, M. Greiner, M. Biesinger, S. Tougaard, D. Morgan, J. Baltrusaitis, Systematic and Collaborative Approach to Problem Solving using X-ray Photoelectron Spectroscopy, Appl. Surf. Sci. Adv. (2021) submitted.

[13] F.L. Bauer, A.S. Householder, J.H. Wilkinson, C. Reinsch, Handbook for Automatic Computation: Volume II: Linear Algebra, Springer, Berlin Heidelberg, 2012.

[14] S. Béchu, M. Richard-Plouet, V. Fernandez, J. Walton, N. Fairley, Developments in numerical treatments for large data sets of XPS images, Surf. Interface Anal. 48 (2016) 301–309. https://doi.org/10.1002/sia.5970.

[15] J. Walton, N. Fairley, Noise reduction in X-ray photoelectron spectromicroscopy by a singular value decomposition sorting procedure, J. Electron Spectros. Relat. Phenomena. 148 (2005) 29–40. https://doi.org/10.1016/j.elspec.2005.02.003.

[16] V. Fernandez, N. Fairley, J. Baltrusaitis, Unraveling spectral shapes of adventitious carbon on gold using a time-resolved high-resolution X-ray photoelectron spectroscopy and principal component analysis, Appl. Surf. Sci. 538 (2021) 148031. https://doi.org/10.1016/j.apsusc.2020.148031.

[17] J.E. Castle, A.M. Salvi, Chemical state information from the near-peak region of the X-ray photoelectron background, J. Electron Spectros. Relat. Phenomena. 114–116 (2001) 1103–1113. https://doi.org/https://doi.org/10.1016/S0368-2048(00)00305-4.

[18] S. Tougaard, Quantitative XPS: non-destructive analysis of surface nano-structures, Appl. Surf. Sci. 100–101 (1996) 1–10. https://doi.org/10.1016/0169-4332(96)00246-2.

[19] P. Swift, Adventitious carbon: the panacea for energy referencing?, Surf. Interface Anal. 4 (1982) 47–51. https://doi.org/10.1002/sia.740040204.

[20] G. Greczynski, L. Hultman, C 1s Peak of Adventitious Carbon Aligns to the Vacuum Level: Dire Consequences for Material's Bonding Assignment by Photoelectron Spectroscopy, ChemPhysChem. 18 (2017) 1507–1512. https://doi.org/10.1002/cphc.201700126.

[21] J. Walton, N. Fairley, The Casa Cookbook Part 2: XPS Image Processing, (2011) 196.